

Extended-FEM for the solid-fluid mixture two-scale problems with BCC and FCC microstructures

Tomohiro Sawada, Shogo Nakasumi and Akira Tezuka*

Process-oriented Computational Applied Mechanics Group, AMRI, National Institute of Advanced Industrial Science and Technology (AIST), 1-2-1 Namiki, Tsukuba, Ibaraki, 305-8564, Japan

Manabu Fukushima and Yu-ichi Yoshizawa

High-performance Component Processing Group, AMRI, National Institute of Advanced Industrial Science and Technology (AIST), 2266-98 Anagahora, Shimo-Shidami, Nagoya, Aichi, 463-8560, Japan

(Received March 1, 2008, Accepted August 15, 2008)

Abstract. An aim of the study is to develop an efficient numerical simulation technique that can handle the two-scale analysis of fluid permeation filters fabricated by the partial sintering technique of small spherical ceramics. A solid-fluid mixture homogenization method is introduced to predict the mechanical characters such as rigidity and permeability of the porous ceramic filters from the micro-scale geometry and configuration of partially-sintered particles. An extended finite element (X-FE) discretization technique based on the enriched interpolations of respective characteristic functions at fluid-solid interfaces is proposed for the non-interface-fitted mesh solution of the micro-scale analysis that needs non-slip condition at the interface between solid and fluid phases of the unit cell. The homogenization and localization performances of the proposed method are shown in a typical two-dimensional benchmark problem whose model has a hole in center. Three-dimensional applications to the body-centered cubic (BCC) and face-centered cubic (FCC) unit cell models are also shown in the paper. The 3D application is prepared toward the computer-aided optimal design of ceramic filters. The accuracy and stability of the X-FEM based method are comparable to those of the standard interface-fitted FEM, and are superior to those of the voxel type FEM that is often used in such complex micro geometry cases.

Keywords: solid-fluid mixtures; porous media; permeation flow; incompressibility; homogenization method; extended finite element method (X-FEM); level set method; fluid-solid interface; ceramic filters; partial sintering.

1. Introduction

With the global expansion of industrial pollutions of air and water of late years, the demand for high efficiency fluid filters continues to grow up as a core components of fluid purification systems, in which they are usually utilized for providing air bubbles into bacteria tanks (i.e. aeration) or directly be used for purifying sewage. Although there are various types of filters, porous ceramic filters fabricated by the partial sintering technique (Greskovich and Lay 1972, Suwanmethanond *et*

* Corresponding Author, E-mail: tezuka.akira@aist.go.jp

et al. 2000, Krenar *et al.* 2006, Fukushima *et al.* 2008) of small ceramic particles or powder (Lin and Burggraaf 1991, Nanjangud and Green 1995, Hardy and Green 1995, Lin and Tsai 1997, Isobe *et al.* 2007) are now widely used as one of the aeration media in the bacteria tanks. Fig. 1 gives an illustration of the partial sintering of the spherical ceramic particles (a) and a X-ray CT (computerized tomography) photomicrograph of the actual microstructure of the particle-type ceramic filter fabricated by the fourth and last authors of this paper (b), respectively. We are now developing an advanced fabrication technique of the particle type filters so that we can give them superior mechanical properties to the existing ones (Fukushima *et al.* 2008). A final target of this collaborative study is to propose a guideline on how to design the particle-type ceramic filters under the existence of trade-off relationships between their permeability and rigidity to the ceramics engineers. We would maximize the permeability in order to obtain high aeration efficiency, but the rigidity should be sufficient for running under the load pressure in the circulating sewage. The trade-off relation is generally an inherent one, because the more the sintering densification illustrated in Fig. 1(a) proceeds, the more the permeability of the filter decreases and the rigidity increases.

To propose the useful guideline of designing it, we introduce a two-scale computational approach based on the asymptotic homogenization method for porous media (Hornung 1997) and solid-fluid mixtures (Terada *et al.* 1998, Murad *et al.* 2001, Wang *et al.* 2003) in grasping the aforementioned relationship between the two mechanical characters. This homogenization method can handle the two-scale analysis of the elastic porous media saturated with an incompressible viscous fluid, and it enables us to evaluate the two characters from the homogenization analysis of periodic microstructure model of it (Takano *et al.* 2002, Sawada *et al.* 2007a, b). In this study, we give the priority to revealing how the rigidity and permeability of the sintered particles change according to the depth of the neck parts of the sintered particles of Fig. 1(a) over the direct evaluation of them from the actual microstructure shown in Fig. 1(b). The body- and face-centered cubic (BCC and FCC) microstructure models are introduced to extract the relation without the undesirable dependence on the random and uncontrolled factors for the ceramics engineers. That is, the role of the CAE in this study is not to evaluate the two characters from actual microstructures, but to grasp their tendencies introducing the idealized models of the actual structures. The direct evaluation technique for the too complex microstructures is studied in Takano *et al.* (2003a, b) and Ikeda *et al.* (2004) using a voxel mesh-like treatment of the actual structures, but only the evaluation technique

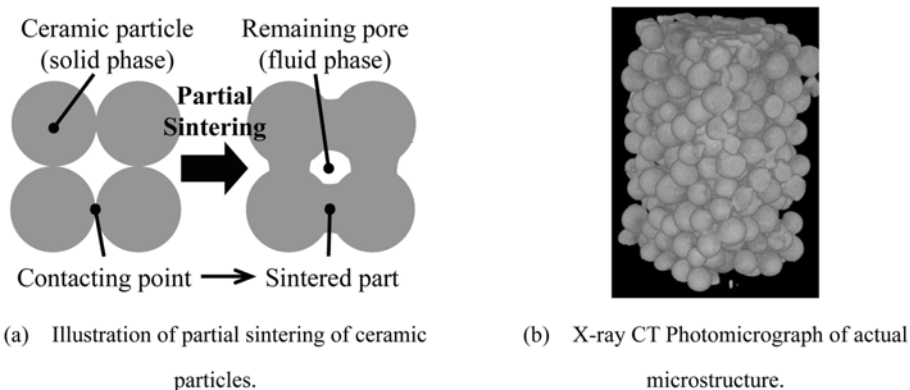


Fig. 1 Porous ceramics filter fabricated by partial sintering of small spherical particles

for the stiffness is discussed in these papers.

In the extraction analysis, it becomes a practical but major obstacle that the solid-fluid mixture homogenization method needs a complex interface-fitted mesh to perform the homogenization analysis of the microstructures, because its unit cell is composed of solid and fluid phases with interfaces, and non-slip velocity conditions are required to be satisfied at the interfaces. Such a situation becomes worse especially in the extraction analysis where we change the depth of the neck parts of Fig. 1(a) by little and little for the purpose of figuring out the trade-off relation. Supposed that these analyses are carried out with the interface-fitted meshes, an appropriate mesh update scheme or adaptive regeneration technique (Johnson and Tezduyar 1999, Stein *et al.* 2003, Sawada and Hisada 2007c) is required to keep the interface-fitted mesh healthy at every numerical evaluation points of the neck depth. Therefore, we propose in this paper an alternative method that can handle the micro-structure analysis without the usage of the interface-fitted meshes. This method is fundamentally based on the eXtended Finite Element Method (X-FEM) that was proposed as the method for handling arbitrary discontinuities in finite elements (Moës *et al.* 1999, Belytschko *et al.* 2001, Wagner *et al.* 2001, Nagashima *et al.* 2003, Legay *et al.* 2006, Sawada *et al.* 2007d). The eXtended finite element method proposed here is able to achieve the two-phase microstructure analysis with a non-interface-fitted mesh. Such an approach is already applied to the heterogeneous structures that have complex microstructure geometries (Moës *et al.* 2003); however, precedent for studying the way of applying the X-FEM to the solid-fluid mixture homogenization method is not reported yet to our best knowledge.

A main computational problem is how to deal with the non-slip velocity condition at the fluid-solid interfaces of the unit cell under the usage of non-interface-fitted meshes. In this study, we introduce a local enrichment function that can satisfy the interface condition without additional constraint equations based on Lagrange-multiplier method or penalty method that are applied generally in such cases (Legay *et al.* 2006, Sawada *et al.* 2007d). With the proposed method, we have succeeded in revealing how the rigidity and permeability changes according to the depth of the neck parts in the case of the idealized BCC and FCC microstructures. This method will also become an effective tool to optimal designs of the ceramic filter in future stage where the shape of the solid and fluid phases changes every iteration (Guest and Prévost 2006), because it does not need to regenerate the unit cell mesh every iteration. Guest and Prévost (2006) solved the problem using a voxel mesh-type approach.

In Section 2, we give a summary of the two-scale asymptotic homogenization method for fluid-solid mixtures used in this study. The original homogenization method developed by Terada *et al.* (1998) is not consistent to the incompressibility of the micro-scale flow in the porous media, so we reformulate the homogenized equations so that they become consistent in both scales based on Wang *et al.* (2003). And then, the extended finite element method, which is developed to discretize the two-phase unit cell using the non-interface-fitted mesh, is described in Section 3. The local enrichments functions introduced here automatically reproduce the fluid-solid interface conditions. Computational performances of the proposed method are demonstrated in a two-dimensional test analysis in Section 4, where the interface-fitted mesh method and voxel-type mesh method are introduced to comparison studies. Three-dimensional applications of the method to the BCC and FCC microstructure models are shown in Section 5, and then the trade-off relations between the rigidity and permeability of the two microstructures are shown at the same time. Conclusions of this study are summarized in Section 6.

2. Homogenization method for solid-fluid mixtures

This section describes the homogenization method for the linear-elasticity porous media saturated with an incompressible viscous fluid used in this study. Several types of the formulation and the solving technique have already been proposed (Hornung 1997, Terada *et al.* 1998, Murad *et al.* 2001, Wang *et al.* 2003). We show the formulation that is consistent to the incompressibility of the fluid in both scales, thus we use the displacement, velocity, and pressure mixed formulation for describing the problem. Governing equations for describing the macroscopic behavior of the porous media are derived from the homogenization method using the two-scale asymptotic expansion of those for microscopic fluid and solid phases. Mechanical interactions between the fluid and solid phases are taken into the formulation via the homogenization technique for the fluid pressure acting at the fluid-solid interface.

2.1 Fundamental equations for two-scale asymptotic expansion

Fig. 2 shows the illustration of the homogenization procedure of the porous media Ω^ε with a periodic microstructure (i.e. unit cell) Y that is composed of solid and fluid phases, Y_s and Y_f . The vectors \mathbf{x} and \mathbf{y} denote the macro- and micro-scale coordinates, respectively. The micro-scale coordinates is introduced to achieve the two-scale asymptotic expansion of the primitive variables of the problem. It is defined as $\mathbf{y} \equiv \mathbf{x}/\varepsilon$ with the representative scale ratio ε between the two coordinates.

Primitive variables of the problem are the velocity $\mathbf{v}^\varepsilon(\mathbf{x})$ and pressure $p^\varepsilon(\mathbf{x})$ of the contained fluid, and the displacement $\mathbf{u}^\varepsilon(\mathbf{x})$ of the porous media. Their superscript ε denotes the dependency on the scale parameter; therefore, they include both the macro- and micro-scale effects. The asymptotic expansion of the three primitive variables is given as follows, respectively:

$$\mathbf{v}^\varepsilon(\mathbf{x}) = \sum_{n=0}^{\infty} \varepsilon^n \mathbf{v}^{(n)}(\mathbf{x}, \mathbf{y}), \quad p^\varepsilon(\mathbf{x}) = \sum_{n=0}^{\infty} \varepsilon^n p^{(n)}(\mathbf{x}, \mathbf{y}) \quad (1a,b)$$

$$\mathbf{u}^\varepsilon(\mathbf{x}) = \sum_{n=0}^{\infty} \varepsilon^n \mathbf{u}^{(n)}(\mathbf{x}, \mathbf{y}) \quad (1c)$$

where $\mathbf{v}^{(n)}(\mathbf{x}, \mathbf{y})$, $p^{(n)}(\mathbf{x}, \mathbf{y})$, and $\mathbf{u}^{(n)}(\mathbf{x}, \mathbf{y})$ are the solutions corresponding to the n -th order of ε .

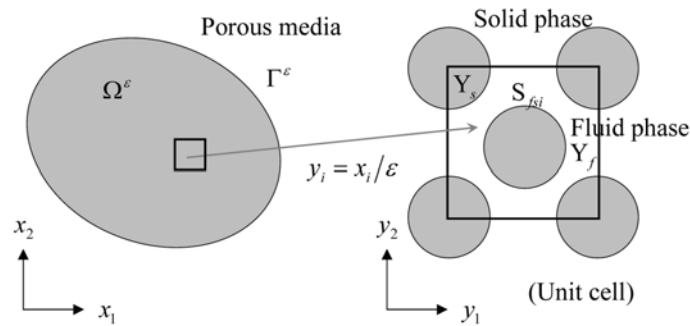


Fig. 2 Homogenization of porous media with a periodic microstructure

All of them have the $\bar{\mathbf{y}}$ -periodicity, where the vector $\bar{\mathbf{y}}$ represents the periodic lengths of the unit cell. The gradient operator ∇^ε and Laplacian $\nabla^\varepsilon \cdot \nabla^\varepsilon$ are divided into the two-scale coordinates according to the chain-rule associated with the scale parameter ε , which result in:

$$\nabla^\varepsilon = \nabla_x + \varepsilon^{-1} \nabla_y, \quad \nabla^\varepsilon \cdot \nabla^\varepsilon = \nabla_x \cdot \nabla_x + 2 \varepsilon^{-1} \nabla_x \cdot \nabla_y + \varepsilon^{-2} \nabla_y \cdot \nabla_y \quad (2a,b)$$

The integration theorems for decoupling the true domain and surface integrals into the two scales are given as follows, respectively:

$$\lim_{\varepsilon \rightarrow 0} \int_{\Omega^\varepsilon} \psi^\varepsilon(\mathbf{x}) d\Omega = \int_{\Omega} \langle \psi(\mathbf{x}, \mathbf{y}) \rangle_Y d\Omega, \quad \lim_{\varepsilon \rightarrow 0} \int_{\Gamma^\varepsilon} \varepsilon \psi^\varepsilon(\mathbf{x}) d\Gamma = \int_{\Omega} \langle \psi(\mathbf{x}, \mathbf{y}) \rangle_S d\Omega \quad (3a,b)$$

where Ω and Γ are the macroscopic domain/volume and surface/area of the homogenized porous media, respectively, and Y and S are those of the unit cell. The function $\psi(\mathbf{x}, \mathbf{y})$ represents the arbitrary scalars, vectors, or tensors with the $\bar{\mathbf{y}}$ -periodicity, and those with the angle bracket $\langle \rangle$ express the volume average of the function in the unit cell domain as follows.

$$\langle \psi(\mathbf{x}, \mathbf{y}) \rangle_{Y_a} \equiv \frac{1}{Y} \int_{Y_a} \psi(\mathbf{x}, \mathbf{y}) dY, \quad \langle \psi(\mathbf{x}, \mathbf{y}) \rangle_{S_a} \equiv \frac{1}{Y} \int_{S_a} \psi(\mathbf{x}, \mathbf{y}) dS \quad (4a,b)$$

where Y_a and S_a are the partial domain and surface of Y , respectively. These notations are introduced for brief descriptions.

2.2 Homogenization of fluid phases

Fluid flow in microscopic pores of the porous media is modeled as the Stokes flow whose Newtonian viscosity is assumed to be defined as $\mu_f^\varepsilon(\mathbf{x}) = \varepsilon^2 \mu_f(\mathbf{y})$ with μ_f corresponding to the micro-scale viscosity (see, Terada *et al.* 1998). The Stokes flow is governed by the following strong form equations:

$$\nabla^\varepsilon \cdot \mathbf{T}_f^\varepsilon + \rho_f \mathbf{g} = \mathbf{0}, \quad \nabla^\varepsilon \cdot \mathbf{v} = 0 \quad \text{in } \Omega_f^\varepsilon \quad (5a,b)$$

$$\mathbf{T}_f^\varepsilon = -p^\varepsilon \mathbf{I} + 2\mu_f^\varepsilon \mathbf{D}^\varepsilon, \quad \mathbf{D}^\varepsilon = \frac{1}{2} \{ (\nabla^\varepsilon \mathbf{v}^\varepsilon) + (\nabla^\varepsilon \mathbf{v}^\varepsilon)^T \} \quad (6a,b)$$

where $\mathbf{T}_f^\varepsilon(\mathbf{x})$ and ρ_f is the Cauchy stress tensor and mass density, respectively, \mathbf{g} the body force density, and \mathbf{I} and $\mathbf{D}^\varepsilon(\mathbf{x})$ are the identity and stretching tensors, respectively. These equations yield the bellow Laplacian form of Eqs. (5):

$$-\nabla^\varepsilon p^\varepsilon(\mathbf{x}) + \mu_f \varepsilon^2 \nabla^\varepsilon \cdot \nabla^\varepsilon \mathbf{v}^\varepsilon(\mathbf{x}) + \rho_f \mathbf{g} = \mathbf{0}, \quad \nabla^\varepsilon \cdot \mathbf{v}(\mathbf{x}) = 0 \quad \text{in } \Omega_f^\varepsilon \quad (7a,b)$$

Eq. (7a) denotes that viscous effects of the incompressible flow becomes negligible in the homogenized behavior of the porous media; i.e., $\lim_{\varepsilon \rightarrow 0} \mu_f^\varepsilon = 0$. The viscosity, therefore, does not appear in the macro-scale governing equation. It appears as the Darcy law for macroscopic permeation given by the homogenization method below. Boundary conditions of Eqs. (7) are assumed to be given as:

$$\mathbf{v}^\varepsilon(\mathbf{x}) = \bar{\mathbf{v}} \quad \text{on } \Gamma_{fv} \setminus \Gamma_{fsi}^\varepsilon, \quad \mathbf{v}^\varepsilon(\mathbf{x}) = \mathbf{0} \quad \text{on } \Gamma_{fsi}^\varepsilon \quad (8a,b)$$

where $\bar{\mathbf{v}}$ is the prescribed velocity at the corresponding fluid boundaries, Γ_{fv} , but except for the fluid-solid interfaces Γ_{fsi}^ε including complex microscopic geometries. In the present method, fluid velocities at the fluid-solid interfaces are treated as a non-slip and their magnitude is zero for matching the interface velocity with the steady state of the solid phase. This condition is written in Eq. (8b).

The two-scale asymptotic expansion of Eqs. (7) requires the below equations using Eqs. (1) and (2):

$$-\nabla_y p^{(0)}(\mathbf{x}, \mathbf{y}) = \mathbf{0}$$

$$\nabla_x \cdot \mathbf{v}^{(0)}(\mathbf{x}, \mathbf{y}) = -\nabla_y \cdot \mathbf{v}^{(1)}(\mathbf{x}, \mathbf{y}) \quad \text{in } \Omega \times Y_f \quad (9a,b)$$

$$-\nabla_y \cdot p^{(1)}(\mathbf{x}, \mathbf{y}) + \mu_f \nabla_y \cdot \nabla_y \cdot \mathbf{v}^{(0)}(\mathbf{x}, \mathbf{y}) = \nabla_x \cdot p^{(0)}(\mathbf{x}, \mathbf{y}) - \rho_f \mathbf{g}$$

$$\nabla_y \cdot \mathbf{v}^{(0)}(\mathbf{x}, \mathbf{y}) = \mathbf{0} \quad \text{in } \Omega \times Y_f \quad (10a,b)$$

From Eqs. (9), we obtain that $p^{(0)}(\mathbf{x}, \mathbf{y})$ is independent from the micro-scale coordinates \mathbf{y} , and the \mathbf{y} -scale volume average of the divergence of $\mathbf{v}^{(0)}(\mathbf{x}, \mathbf{y})$ becomes zero because of the $\bar{\mathbf{y}}$ -periodicity of $\mathbf{v}^{(1)}(\mathbf{x}, \mathbf{y})$. These are written as:

$$p^{(0)} = p^{(0)}(\mathbf{x}), \quad \nabla_x \cdot \langle \mathbf{v}^{(0)}(\mathbf{x}, \mathbf{y}) \rangle_{Y_f} = 0 \quad \text{in } \Omega \quad (11a,b)$$

Thus, we cannot obtain the independence of $\mathbf{v}^{(0)}(\mathbf{x}, \mathbf{y})$ from the micro-scale coordinates \mathbf{y} in this homogenization problem, and then Eq. (11b) governs the macroscopic flow in the porous media as a permeation.

Characteristic functions introduced here for decoupling the dependency of the micro-scale velocity $\mathbf{v}^{(0)}(\mathbf{x}, \mathbf{y})$ and pressure $p^{(1)}(\mathbf{x}, \mathbf{y})$ on the both scale coordinates are defined as follows, respectively (Wang *et al.* 2003):

$$\mathbf{v}^{(0)}(\mathbf{x}, \mathbf{y}) = -\mathbf{K}(\mathbf{y}) \cdot (\nabla_x p^{(0)}(\mathbf{x}) - \rho_f \mathbf{g}) \quad \text{in } \Omega \times Y_f \quad (12a)$$

$$p^{(1)}(\mathbf{x}, \mathbf{y}) = -\boldsymbol{\lambda}(\mathbf{y}) \cdot (\nabla_x p^{(0)}(\mathbf{x}) - \rho_f \mathbf{g}) \quad \text{in } \Omega \times Y_f \quad (12b)$$

The function $\mathbf{K}(\mathbf{y})$ is defined as the fluid velocity tensor in the unit-cell that is composed of the three characteristic velocity vectors $\boldsymbol{\kappa}^k(\mathbf{y})$ ($k=1, 2, 3$) under the action of the macroscopic unit pressure gradient of \mathbf{e}_k -direction. The function $\boldsymbol{\lambda}(\mathbf{y})$ is composed of the three characteristic pressures $\lambda^k(\mathbf{y})$ ($k=1, 2, 3$) in the same manner. These definitions are written as follows using the orthonormal bases \mathbf{e}_k :

$$\mathbf{K}(\mathbf{y}) \equiv \boldsymbol{\kappa}^k \circ \mathbf{e}_k, \quad \boldsymbol{\lambda}(\mathbf{y}) \equiv \lambda^k \mathbf{e}_k \quad (13a,b)$$

where the operator \circ is introduced to denote the tensor product. Using Eq. (12a), we can define the homogenized velocity $\mathbf{v}^H(\mathbf{x})$ below that reproduces the macroscopic permeation velocity:

$$\mathbf{v}^H(\mathbf{x}) \equiv \langle \mathbf{v}^{(0)}(\mathbf{x}, \mathbf{y}) \rangle_{Y_f} = -\mathbf{K}^H \cdot (\nabla_x p^{(0)}(\mathbf{x}) - \rho_f \mathbf{g}) \quad \text{in } \Omega \quad (14)$$

with the homogenized characteristic tensor below, which determines the macroscopic permeability:

$$\mathbf{K}^H \equiv \langle \mathbf{K}(\mathbf{y}) \rangle_{Y_f} \quad (15)$$

From these equations, a homogenized governing equation of the macroscopic behaviors of the flow is given as follows in a strong form:

$$-\nabla_x \cdot (\mathbf{K}^H \cdot \nabla_x p^{(0)}(\mathbf{x})) = 0 \quad \text{in } \Omega \quad (16)$$

in the weak form:

$$\int_{\Omega} \nabla_x \delta p^{(0)}(\mathbf{x}) \cdot \mathbf{K}^H \cdot \nabla_x p^{(0)}(\mathbf{x}) d\Omega = - \int_{\Gamma_v} \delta p^{(0)}(\mathbf{x}) (\bar{\mathbf{v}} \cdot \mathbf{n}) d\Gamma \quad (17)$$

where $\bar{\mathbf{v}} \cdot \mathbf{n}$ is the flux of the permeation at the macroscopic boundary Γ_v resulted from Eq. (8a), and \mathbf{n} is the unit normal vector of the surface. We use the weak form for solving the problem because of the usage of the finite element discretization. Eq. (10) give the following equations governing the two characteristic functions, which in a strong form:

$$\nabla_y \lambda^k(\mathbf{y}) - \mu_f \nabla_y \cdot \nabla_y \boldsymbol{\kappa}^k(\mathbf{y}) = \mathbf{e}_k, \quad \nabla_y \cdot \boldsymbol{\kappa}^k(\mathbf{y}) = 0 \quad \text{in } Y_f \quad (18a,b)$$

in a weak form:

$$\begin{aligned} & - \int_{Y_f} (\nabla_y \cdot \delta \boldsymbol{\kappa}^k(\mathbf{y})) \lambda^k(\mathbf{y}) dY + \int_{Y_f} \nabla_y^S \cdot \delta \boldsymbol{\kappa}^k(\mathbf{y}) : 2\mu_f \nabla_y^S \boldsymbol{\kappa}^k(\mathbf{y}) dY \\ & + \int_{Y_f} \delta \lambda^k(\mathbf{y}) (\nabla_y \cdot \boldsymbol{\kappa}^k(\mathbf{y})) dY = \int_{Y_f} \delta \boldsymbol{\kappa}^k(\mathbf{y}) \cdot \mathbf{e}_k dY \end{aligned} \quad (19)$$

This equation is solved with the zero characteristic velocity condition written in Eq. (8b) at the solid-fluid interfaces of the unit cell S_{fsi} . The gradient operator with the superscript S has been introduced to denote the symmetric form of it.

2.3 Homogenization of solid phases

For describing the deformation of the porous media with permeation flow, we assume that it is governed by the linear-elasticity with infinitesimal strains. Governing equations of the deformation are written as follows in a strong form:

$$\nabla^\varepsilon \cdot \mathbf{T}_s^\varepsilon + \rho_s \mathbf{g} = \mathbf{0} \quad \text{in } \Omega_s^\varepsilon \quad (20)$$

$$\mathbf{T}_s^\varepsilon = (\lambda_s \text{tr} \mathbf{E}^\varepsilon) \mathbf{I} + 2\mu_s \mathbf{E}^\varepsilon \equiv \mathbf{C} : \mathbf{E}^\varepsilon, \quad \mathbf{E}^\varepsilon = \frac{1}{2} \{ (\nabla^\varepsilon \mathbf{u}^\varepsilon) + (\nabla^\varepsilon \mathbf{u}^\varepsilon)^T \} \quad (21a,b)$$

where $\mathbf{T}_s^\varepsilon(\mathbf{x})$ and ρ_s are the Cauchy stress and mass density of the solid, respectively, $\mathbf{E}^\varepsilon(\mathbf{x})$ the linear part of the Green-Lagrange strain, and λ_s and μ_s are the Lamé constants. The tensor \mathbf{C} is the fourth-order tensor introduced for a brief notation of the constitutive equation. The two constants are associated with the Young's modulus E_s and Poisson's ration ν_s in the infinitesimal strain condition as follows:

$$\lambda_s = \nu_s E_s / (1 + \nu_s)(1 - 2\nu_s), \quad \mu_s = E_s / 2(1 + \nu_s) \quad (22a,b)$$

Boundary conditions of Eq. (20) are assumed to be given as:

$$\mathbf{u}^\varepsilon(\mathbf{x}) = \bar{\mathbf{u}} \quad \text{on } \Gamma_{su} \setminus \Gamma_{fsi}^\varepsilon, \quad \mathbf{T}_s^\varepsilon(\mathbf{x}) \cdot \mathbf{n}_s = \bar{\mathbf{t}}_s \quad \text{on } \Gamma_{st} \setminus \Gamma_{fsi}^\varepsilon \quad (23a,b)$$

$$\mathbf{T}_s^\varepsilon(\mathbf{x}) \cdot \mathbf{n}_s = \mathbf{t}_{fsi}^\varepsilon(\mathbf{x}) = -p^\varepsilon(\mathbf{x})\mathbf{n}_s \quad \text{on } \Gamma_{fsi}^\varepsilon \quad (23c)$$

where $\bar{\mathbf{u}}$ and $\bar{\mathbf{t}}_s$ are the prescribed displacement and surface force at the corresponding boundaries. In this homogenization method, fluid-solid coupling effects on the microscopic fluid-solid interfaces become the normal force loaded from the fluid phase pressure $p^\varepsilon(\mathbf{x})$, taking into account of the ε^2 order fluid viscosity. This condition is written in Eq. (23c).

A weak formulation of the boundary value problem is given as follows:

$$\int_{\Omega^\varepsilon} \delta \mathbf{E}^\varepsilon(\mathbf{x}) : \mathbf{T}_s^\varepsilon(\mathbf{x}) d\Omega - \int_{\Gamma_{fsi}^\varepsilon} \delta \mathbf{u}^\varepsilon(\mathbf{x}) \cdot \mathbf{t}_{fsi}^\varepsilon(\mathbf{x}) d\Gamma = \int_{\Omega^\varepsilon} \delta \mathbf{u}^\varepsilon(\mathbf{x}) \cdot \rho_s \mathbf{g} d\Omega + \int_{\Gamma_{st} \setminus \Gamma_{fsi}^\varepsilon} \delta \mathbf{u}^\varepsilon(\mathbf{x}) \cdot \bar{\mathbf{t}}_s(\mathbf{x}) d\Gamma \quad (24)$$

whose two-scale asymptotic expansion requires:

$$\begin{aligned} & \varepsilon^{-2} \int_{\Omega} \langle \delta \mathbf{E}^{(-1)} : \mathbf{T}_s^{(-1)} \rangle_{Y_s} d\Omega + \varepsilon^{-1} \int_{\Omega} \langle \delta \mathbf{E}^{(-1)} : \mathbf{T}_s^{(0)} + \delta \mathbf{E}^{(0)} : \mathbf{T}_s^{(-1)} \rangle_{Y_s} + \langle \delta \mathbf{u}^{(0)} \cdot p^{(0)} \mathbf{n}_s \rangle_{S_{fsi}} d\Omega \\ & + \int_{\Omega} \langle \delta \mathbf{E}^{(-1)} : \mathbf{T}_s^{(-1)} + \delta \mathbf{E}^{(0)} : \mathbf{T}_s^{(0)} + \delta \mathbf{E}^{(1)} : \mathbf{T}_s^{(-1)} \rangle_{Y_s} + \langle \delta \mathbf{u}^{(0)} \cdot p^{(1)} \mathbf{n}_s + \delta \mathbf{u}^{(1)} \cdot p^{(0)} \mathbf{n}_s \rangle_{S_{fsi}} d\Omega \\ & = \int_{\Omega^\varepsilon} \langle \delta \mathbf{u}^{(0)} : \rho_s \mathbf{g} \rangle_{Y_s} d\Omega + \int_{\Gamma_{st} \setminus \Gamma_{fsi}^\varepsilon} \delta \mathbf{u}^{(0)} \cdot \bar{\mathbf{t}}_s d\Gamma \end{aligned} \quad (25)$$

with the below respective order strain and stress tensors:

$$\mathbf{E}^{(-1)} = \nabla_y^S \mathbf{u}^{(0)}, \quad \mathbf{E}^{(0)}(\mathbf{x}, \mathbf{y}) = \nabla_x^S \mathbf{u}^{(0)} + \nabla_y^S \mathbf{u}^{(1)}, \quad \mathbf{E}^{(1)}(\mathbf{x}, \mathbf{y}) = \nabla_x^S \mathbf{u}^{(1)} + \nabla_y^S \mathbf{u}^{(2)} \quad (26a,b,c)$$

$$\mathbf{T}_s^{(-1)} = \mathbf{C} : \mathbf{E}^{(-1)}, \quad \mathbf{T}_s^{(0)}(\mathbf{x}, \mathbf{y}) = \mathbf{C} : \mathbf{E}^{(0)}, \quad \mathbf{T}_s^{(1)}(\mathbf{x}, \mathbf{y}) = \mathbf{C} : \mathbf{E}^{(1)} \quad (27a,b,c)$$

From the ε^{-2} order term of Eq. (25) and the fact that the constitutive tensor \mathbf{C} is a positive defined, we obtain the independence of $\mathbf{u}^{(0)}(\mathbf{x}, \mathbf{y})$ from the micro-scale coordinates \mathbf{y} , which is written as $\mathbf{u}^{(0)} = \mathbf{u}^{(0)}(\mathbf{x})$. Thus, that of the order ε^{-1} is all vanished owing to the $\bar{\mathbf{y}}$ -periodicity as follows:

$$0 + 0 + \langle \delta \mathbf{u}^{(0)}(\mathbf{x}) \cdot p^{(0)}(\mathbf{x}) \mathbf{n}_s \rangle_{S_{fsi}} = \delta \mathbf{u}^{(0)}(\mathbf{x}) p^{(0)}(\mathbf{x}) \cdot \langle \mathbf{n}_s \rangle_{S_{fsi}} = 0 \quad (28)$$

The fluid-solid interface conditions with the ε^0 order are transformed as follows using the divergence theorem and the $\bar{\mathbf{y}}$ -periodicities of $p^{(1)}(\mathbf{x}, \mathbf{y})$ and $\delta \mathbf{u}^{(1)}(\mathbf{x}, \mathbf{y})$:

$$\begin{aligned} & \int_{\Omega} \langle \delta \mathbf{u}^{(0)}(\mathbf{x}) \cdot p^{(1)}(\mathbf{x}, \mathbf{y}) \mathbf{n}_s + \delta \mathbf{u}^{(1)}(\mathbf{x}, \mathbf{y}) \cdot p^{(0)}(\mathbf{x}) \mathbf{n}_s \rangle_{S_{fsi}} d\Omega \\ & = \int_{\Omega} \delta \mathbf{u}^{(0)}(\mathbf{x}) \cdot \langle \nabla_y p^{(1)}(\mathbf{x}, \mathbf{y}) \rangle_{Y_s} + \langle (\nabla_y \cdot \delta \mathbf{u}^{(1)}(\mathbf{x}, \mathbf{y})) p^{(0)}(\mathbf{x}) \rangle_{Y_s} d\Omega \end{aligned} \quad (29)$$

This equation denotes that the effect of $p^{(1)}(\mathbf{x}, \mathbf{y})$ does not appear in the homogenized governing equation for micro-scale. From these results, the terms associated with ε^0 are decomposed into the below macro- and micro-scale governing equations of the problem:

$$\int_{\Omega} \nabla_x^S \delta \mathbf{u}^{(0)} : \langle \mathbf{T}_s^{(0)} \rangle_{Y_s} d\Omega = \int_{\Omega} \delta \mathbf{u}^{(0)} \cdot \langle \rho_s \rangle_{Y_s} \mathbf{g} d\Omega + \int_{\Gamma_{st} \cup \Gamma_{fsi}^{\varepsilon}} \delta \mathbf{u}^{(0)} \cdot \bar{\mathbf{t}}_s d\Gamma \quad (30)$$

$$\langle \nabla_y^S \delta \mathbf{u}^{(1)}(\mathbf{x}, \mathbf{y}) : \mathbf{T}_s^{(0)}(\mathbf{x}, \mathbf{y}) + (\nabla_y \cdot \delta \mathbf{u}^{(1)}(\mathbf{x}, \mathbf{y})) p^{(0)}(\mathbf{x}) \rangle_{Y_s} = 0 \quad (31)$$

where Eq. (26b) and the $\bar{\mathbf{y}}$ -periodicity that yields $\langle \nabla_y p^{(1)}(\mathbf{x}, \mathbf{y}) \rangle_{Y_s} = 0$ have already been substituted.

Characteristic functions introduced here for $\mathbf{u}^{(1)}(\mathbf{x}, \mathbf{y})$ are defined as follows (Terada *et al.* 1998):

$$\mathbf{u}^{(1)}(\mathbf{x}, \mathbf{y}) = -\boldsymbol{\varphi}(\mathbf{y}) p^{(0)}(\mathbf{x}) - \mathbf{X}(\mathbf{y}) : \mathbf{E}^H(\mathbf{x}) \quad \text{in } \Omega \times Y_s \quad (32)$$

where $\boldsymbol{\varphi}(\mathbf{y})$ is the characteristic displacement for the macro pressure $p^{(0)}(\mathbf{x})$, and $\mathbf{X}(\mathbf{y})$ is that for the macro strain $\mathbf{E}^H(\mathbf{x})$ given as the bellow volume average:

$$\mathbf{E}^H(\mathbf{x}) \equiv \langle \mathbf{E}^{(0)}(\mathbf{x}, \mathbf{y}) \rangle_{Y_s} = \nabla_x^S \mathbf{u}^{(0)}(\mathbf{x}) \quad (33)$$

The characteristic function $\mathbf{X}(\mathbf{y})$ can be defined as the third order tensor composed of the nine characteristic displacement vectors $\boldsymbol{\chi}^{kh}(\mathbf{y})$ for each stain component $E_{kh}^H(\mathbf{x})$ ($k, h = 1, 2, 3$), but the fundamental components of $\boldsymbol{\chi}^{kh}(\mathbf{y})$ are only the six components corresponding to $k, h = 11, 22, 33, 12, 23, 31$ because of the symmetricity of the strain tensor. Then, the tensor notation of $\mathbf{X}(\mathbf{y})$ is written as:

$$\mathbf{X}(\mathbf{y}) \equiv \boldsymbol{\chi}^{kh} \circ \mathbf{e}_k \circ \mathbf{e}_h \quad (34)$$

From these equations, the homogenized equation derive form Eq. (30) is given as follows. This equation governs the macro-scale deformation of the porous media:

$$\begin{aligned} & - \int_{\Omega} \nabla_x^S \delta \mathbf{u}^{(0)}(\mathbf{x}) : \mathbf{Q}^H p^{(0)}(\mathbf{x}) d\Omega + \int_{\Omega} \nabla_x^S \delta \mathbf{u}^{(0)}(\mathbf{x}) : \mathbf{C}^H : \nabla_x^S \mathbf{u}^{(0)}(\mathbf{x}) d\Omega \\ & = \int_{\Omega} \delta \mathbf{u}^{(0)}(\mathbf{x}) : \rho^H \mathbf{g} d\Omega + \int_{\Gamma_{st} \cup \Gamma_{fsi}^{\varepsilon}} \delta \mathbf{u}^{(0)}(\mathbf{x}) \cdot \bar{\mathbf{t}}_s d\Gamma \end{aligned} \quad (35)$$

with the below homogenized matrices that define the macroscopic material properties of the porous media:

$$\mathbf{C}^H = \langle \mathbf{C} : (\mathbf{e}_k \circ \mathbf{e}_h - \nabla_y^S \boldsymbol{\chi}^{kh}) \rangle_{Y_s}, \quad \mathbf{Q}^H = \langle \mathbf{C} \cdot \nabla_y^S \boldsymbol{\varphi} \rangle_{Y_s}, \quad \rho^H = \langle \rho_s \rangle_{Y_s} \quad (36a,b,c)$$

The tensor \mathbf{C}^H is the homogenized elasticity tensor for macro-scale deformation, \mathbf{Q}^H is that of pressure, and ρ^H the homogenized mass density. The first term of Eq. (35) is the coupling term of the fluid permeation pressure and the solid deformation, and the solution of the 0-th order pressure $p^{(0)}(\mathbf{x})$ is obtained by solving Eq. (17). The second term corresponds to the ordinary homogenized elasticity. And, governing equations for the two characteristic functions are given as follows using Eqs. (31) and (32), respectively:

$$\int_{Y_s} \nabla_y^S \delta \boldsymbol{\chi} : (\mathbf{e}_k \circ \mathbf{e}_h - \nabla_y^S \boldsymbol{\chi}^{kh}) dY = 0, \quad \int_{Y_s} \nabla_y^S \delta \boldsymbol{\varphi} : (\mathbf{I} - \mathbf{C} : \nabla_y^S \boldsymbol{\varphi}) dY = 0 \quad (37a,b)$$

As a notice for the homogenization method, the simultaneous equations constructed by Eqs. (17) and (35) coincide with those derived from the classical two-phase theory for solid-fluid mixtures (Biot 1956); however, in this homogenization method every material properties of the equation are evaluated with Eqs. (15) and (36) via the micro-scale (unit-cell) analysis.

3. X-FEM for solid-fluid two-phase microstructures

The solid-fluid mixture homogenization method described in Section 2 generally needs an interface-fitted finite element mesh for solving the microstructure model (i.e., unit cell) of the porous media (Terada *et al.* 1998, Takano *et al.* 2002). The interface-fitted method is required to discretize the fluid and solid phases respectively, and to prescribe the non-slip velocity conditions at the interface via the node-base essential boundary condition. In this section, we describe an alternative approach based on the eXtended finite element method (X-FEM) (Moës *et al.* 1999, Belytschko *et al.* 2001, Legay *et al.* 2006, Sawada *et al.* 2007d) that is developed to discretize the two-phase unit cell without the usage of interface-fitted meshes. This approach in particular is suitable for meeting our demand for grasping how the macroscopic material properties represented by rigidity and permeability of the porous media change according to the depth of sintered parts of the ceramic particles as shown in Fig. 1(a) (Sawada *et al.* 2007a,b).

3.1 Level-set representation of fluid-solid interface

The method proposed here introduces local enrichments to the finite element interpolation spaces of the respective characteristic functions for fluid velocities, pressures, and solid displacements across the fluid-solid interfaces in the unit cell. The local enrichments give the non-interface-fitted mesh the capability of reproducing not only the discontinuity of the three primitive variables but also the non-slip velocity condition at the interfaces. Fig. 3 gives a simple two-dimensional illustration of the non-interface-fitted finite elements around the fluid-solid interface in the unit cell. The white and black square nodes in Fig. 3 are the standard fluid and solid nodes without enrichment, respectively. The gray nodes are the enriched ones that construct finite elements crossing the fluid-solid interface of the two-phase unit cell.

Respective enrichment functions for the characteristic velocities $\boldsymbol{\kappa}^k(\mathbf{y})$ and pressures $\lambda^k(\mathbf{y})$ of the fluid phase ($k=1, 2, 3$), and those for the displacements $\boldsymbol{\chi}^{kh}(\mathbf{y})$, $\boldsymbol{\varphi}(\mathbf{y})$ of the solid phase ($kh=11, 22, 33, 12, 23, 31$), are determined by the level set method using the below signed distance function $f(\mathbf{y})$. The level set function is constructed so that the domain of $f > 0$ corresponds to the fluid phases Y_f , $f < 0$ to the solid phases Y_s , and $f = 0$ to the fluid-solid interfaces S_{fsi} as shown in Fig. 3.

$$f(\mathbf{y}) = \sum_{a \in Q} N_a(\mathbf{y}) f_a \quad \text{in } Q \quad (38)$$

$$f_a = \min_{y_{fsi} \in S_{fsi}} \|\mathbf{y}_a - \mathbf{y}_{fsi}\| \cdot \text{sign}\{\mathbf{n}_{fsi}^+ \cdot (\mathbf{y}_a - \mathbf{y}_{fsi})\} \quad \text{in } Y \quad (39)$$

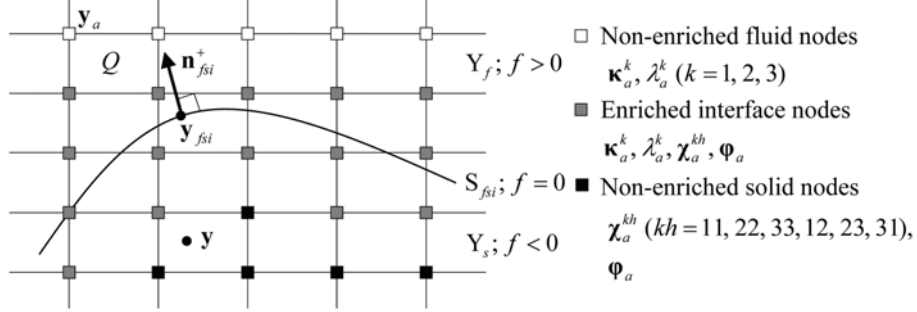


Fig. 3 Two-dimensional illustration of fluid-solid interface and non-interface-fitted finite elements

where f_a is the nodal values of the level set function, $N_a(\mathbf{y})$ the finite element shape functions, \mathbf{y}_{fsi} the arbitrary spatial position vector at the fluid-solid interface S_{fsi} , and \mathbf{n}_{fsi}^+ is the unit normal vector pointing the fluid phase from the position \mathbf{y}_{fsi} . Q expresses one finite element of the unit cell mesh. The combination of Eqs. (38) and (39) decreases the computational cost of the level set function as compared to the following direct evaluation of $f(\mathbf{y})$ without the finite element approximation of Eq. (38):

$$f_a = \min_{\mathbf{y}_{fsi} \in S_{fsi}} \|\mathbf{y} - \mathbf{y}_{fsi}\| \cdot \text{sign}\{\mathbf{n}_{fsi}^+ \cdot (\mathbf{y} - \mathbf{y}_{fsi})\} \quad \text{in } Y \quad (40)$$

3.2 Local enrichment functions around fluid-solid interface

In order to give the non-interface-fitted mesh the capability of reproducing the sharp discontinuity of the four characteristic functions at the fluid-solid interfaces, we introduce the step- and edge-type enrichment functions defined as:

$$f_{step}^+(\mathbf{y}) = \begin{cases} 1 & (f \geq 0) \\ 0 & (f < 0) \end{cases} \quad (41)$$

$$f_{step}^-(\mathbf{y}) = \begin{cases} 1 & (f \geq 0) \\ 0 & (f < 0) \end{cases} \quad (42)$$

$$f_{edge}^+(\mathbf{y}) = \begin{cases} 1 & (f_a \leq f) \\ |f(\mathbf{y})| / |f_a| & (0 \leq f < f_a) \\ 0 & (f < 0) \end{cases} \quad (43)$$

The enrichment function $f_{step}^+(\mathbf{y})$ is the typical step function that jumps from one to zero sharply at the fluid-solid interface. When the superscript of $f_{step}^+(\mathbf{y})$ is plus as is the case of Eq. (41), the step function defines the enriched variables only in the fluid phases. By contrast, when it is minus as Eq. (42), it is defined only in the solid phases. The enrichment function $f_{edge}^+(\mathbf{y})$ defined in Eq. (43) is the one-side edge-type function that is introduced to make the fluid velocities at the interfaces satisfy the non-slip velocity condition with a zero value. The edge function is equal to

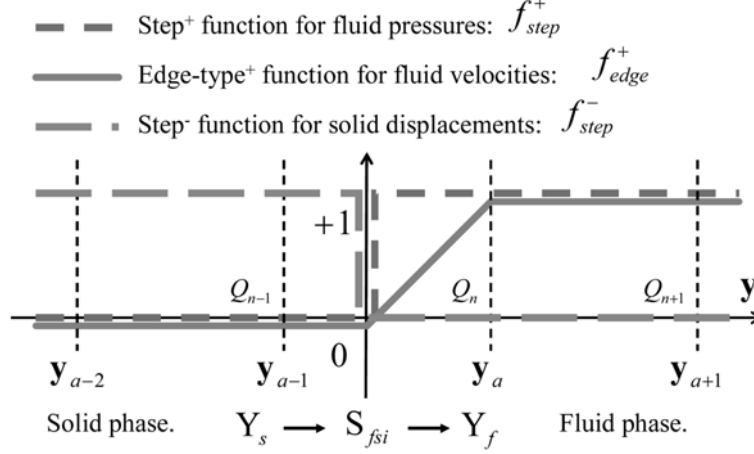


Fig. 4 Step- and edge-type enrichment functions around solid-fluid interface

one almost in the fluid phase, but it becomes linearly to zero at the fluid-solid interface from the fluid nodes that construct fluid finite elements crossing the interface. These enrichment functions are illustrated in Fig. 4 as a simple one-dimensional example.

3.4 Enriched interpolations at fluid-solid interface

Extended interpolations for the respective characteristic functions for velocity and pressure of the fluid phase, and those for displacement of the solid phase are given as follows, respectively:

$$\boldsymbol{\kappa}^k(\mathbf{y}) = f_{edge}^+(\mathbf{y}) \sum_{a \in Q} N_a(\mathbf{y}) \boldsymbol{\kappa}_a^k \quad (k = 1, 2, 3) \quad (44)$$

$$\lambda^k(\mathbf{y}) = f_{step}^+(\mathbf{y}) \sum_{a \in Q} N_a(\mathbf{y}) \lambda_a^k \quad (k = 1, 2, 3) \quad (45)$$

$$\boldsymbol{\chi}^{kh}(\mathbf{y}) = f_{step}^-(\mathbf{y}) \sum_{a \in Q} N_a(\mathbf{y}) \boldsymbol{\chi}_a^{kh} \quad (kh = 11, 22, 33, 12, 23, 31) \quad (46)$$

$$\boldsymbol{\varphi}(\mathbf{y}) = f_{step}^-(\mathbf{y}) \sum_{a \in Q} N_a(\mathbf{y}) \boldsymbol{\varphi}_a \quad (47)$$

where the scalars and vectors with the subscript α denote the nodal values of them; for instance, the vectors $\boldsymbol{\kappa}_a^k$ are nodal values of the characteristic velocity vectors $\boldsymbol{\kappa}^k(\mathbf{y})$. With the appropriately-selected local enrichment functions, the characteristic velocities and pressure are defined only in the fluid phases, while those for the displacement are only in the solid phase, even if the non-interface-fitted mesh is used for the discretization. Fig. 5 shows how the linear interpolation is modified by the two enrichment functions, $f_{step}^+(\mathbf{y})$ and $f_{edge}^+(\mathbf{y})$, in a simple one-dimensional case. The non-slip velocity condition required to be satisfied at the fluid-solid interface is reproduced exactly by the enrichment function $f_{edge}^+(\mathbf{y})$ without any manipulations of nodal characteristic velocities around the interface. This is the main advantage as compared to the Lagrange multiplier-based methods that requires additional constraint equations to reproduce the zero-velocity condition.

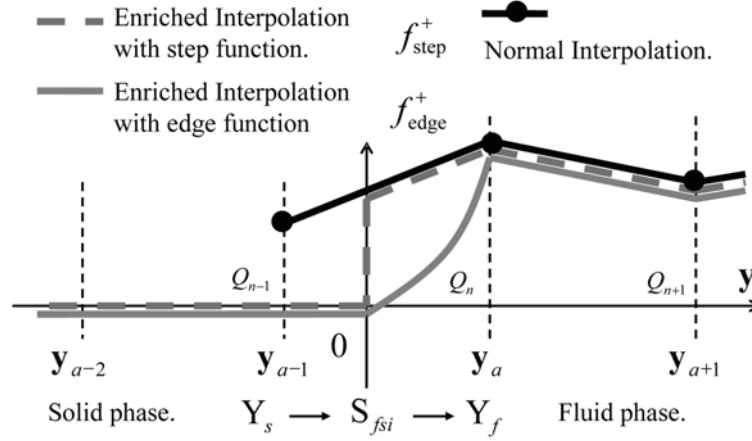


Fig. 5 Locally-enriched interpolations with step- and edge-type functions

3.5 Equal order interpolation of velocity and pressure

As is the case of Fig. 5, we use the Q1 element that has linear category shape functions N_I for the eXtended finite element interpolation of all characteristic functions. The Q1 element degenerates into the two-node line element in one-dimensional cases such as Fig. 5. In two-dimensional cases, it corresponds to the four-node quadrilateral element with bi-linear shape functions, and it becomes the eight-node hexahedral element with tri-linear shape functions in three-dimensional cases. For relaxing the locking phenomena that arises from the usage of equal-order interpolation element (i.e. Q1Q1 element) in solving the velocity and pressure mixed formulation with incompressibility constraints, the pressure-stabilizing/ Petrov-Galerkin (PSPG) formulation (Tezduyar *et al.* 1992, Tezduyar 2003) is applied as the Petrov-Galerkin form of Eq. (19). This stabilization technique enables us to use the Q1Q1 element in the V/P formulation for incompressible flow.

4. Performance assessments of interfacial enrichments

In this section, we compare the localization and homogenization performances of the following three methods in order to demonstrate the computational advantages of the proposed eXtended finite element approach. The first method is the standard finite element method (S-FEM) using an simple interface-fitted mesh, the second is the voxel-type method (V-FEM) whose mesh does not fit the interface exactly, and the last is the proposed method (X-FEM) that introduces the local enrichments at the interfaces.

4.1 Problem set-up

Performance comparison among the three methods is carried out with a two-dimensional square unit cell with a circular hole at center. Fig. 6 shows the finite element meshes of each method, where only the quarter parts of the respective meshes are shown taking account of their axisymmetrical geometry. The V-FEM and X-FEM adopt the uniform rectangular mesh as shown in

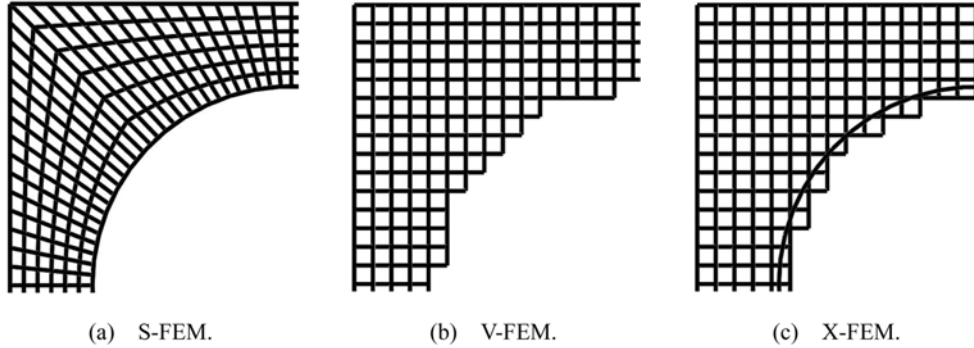


Fig. 6 Three type finite element meshes for two-dimensional benchmark analysis

the corresponding figures (b) and (c). Finite elements per side are 30 for all methods. The side length of the unit cell is $\sqrt{2}$ mm, and the diameter of the center hole D is 1 mm. With respect to the V-FEM, we decide whether or not each element crossing the surface of the inner hole should be included to the homogenization and localization analysis according to the in-and-out side judgment of the center of the gravity of the elements as a commonly used voxel-type approximation. In the benchmark analysis, we apply the periodic conditions at the outside boundaries of the unit cell. Essential boundary conditions with the zero nodal velocity are prescribed to the S-FEM and to the V-FEM at the nodes of the inside boundary of the mesh, while such boundary conditions are not applied to the X-FEM near the inside boundary, because the non-slip condition is satisfied with the introduced edge-type enrichment function.

Using the finite element meshes, we carry out the homogenization and localization analyses of fluid and solid terms both in the same domain (i.e. the outside domain of the inner hole), although the actual solid phase is the inner domain of the circle. The reason for doing this is that the homogenization results for the solid rigidity become undefined (i.e. zero) when the solid phase is analyzed in the hole area due to no existence of periodicity conditions. In this case, the solid phase becomes an floating object in the fluid, which results in zero stiffness. This treatment exerts no inconsistency on the performance assessment, because the fluid and solid phases are decoupled in the homogenization and localization process of the present homogenization method (Terada *et al.* 1998). Young's modulus and Poisson's ratio of the solid phase are 420 GPa and 0.25, respectively, referring to the representative value of alumina ceramics. Viscosity of the fluid is that of the ordinary air: 18.22 mPa s.

4.2 Localization performance

As a localization example, we prescribe the macro pressure $p^{(0)}$ 500 Pa for the localization of the solid, and the macro pressure gradient $\partial p^{(0)} / \partial x_i = 100$ Pa/cm ($i = 1, 2$) for the fluid. These values correspond to those that are supposed to be under the actual circumstance of our ceramic filters under development. Von Mises stresses obtained with the localized solution of the microscopic displacement of Eq. (32) are shown in Fig. 7 for the three methods (S-FEM, V-FEM, and X-FEM). Microscopic velocity norms obtained by Eq. (12a) with the characteristic velocities are shown in Fig. 8. Magnitude of the deformation of the localization analysis is slight, because the prescribed

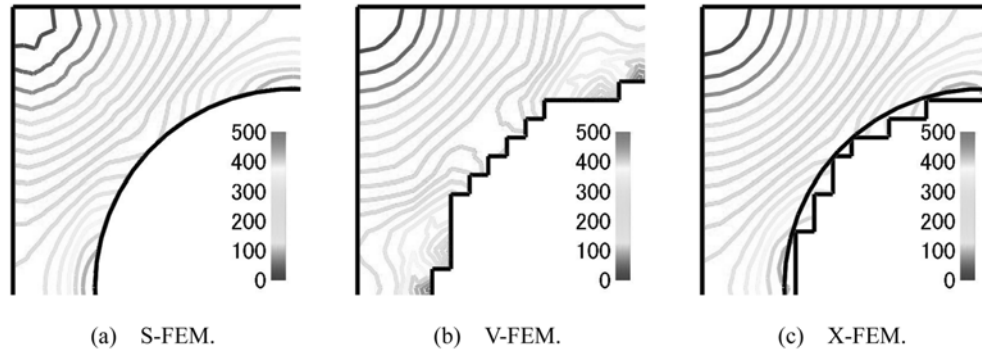


Fig. 7 Colored norm contours of localized solid von Mises stress (Pa)

pressure is negligible in the deformation sense of the alumina.

In Fig. 7, it is observed that the distribution of the von Mises stress of the X-FEM (c) is nearly equal to that of S-FEM (a) with a sufficiently smooth solution around the interface in spite of using a non-interface-fitted mesh in the analysis. This is one of the essential merits of introducing the local enrichments for characteristic displacements. In contrast to the smoothness of the X-FEM solution, that of the V-FEM (b) solution is disturbed due to the voxel mesh treatment, and the inappropriate stress concentration is observed in the vicinity of the interface. From the microscopic design of ceramic filters, the V-FEM does not meet the design demand that we want to grasp concentration of the von Mises stress as possible as exactly that becomes an indicator of plasticity failures and fatigues. From the detailed observation of the stress contours, that of the S-FEM (a) shows the tendency to become gradually unsmooth as close to the corner of the unit cell due to the increase of the aspect ratio of the finite elements, while the X-FEM (c) keeps a smooth contour if the area is close to the corner. This result indicates that the X-FEM is able to surpass the S-FEM in such situations (Terada *et al.* 2003, Terada and Kurumatani 2004), because all area is discretized by the uniform rectangular mesh in the X-FEM. The numerical result of the S-FEM, however, can be enhanced further if the adaptive mesh generation is applied to the inner hole problem.

In Fig. 8, it is observed that the norm contour of the fluid velocity of the X-FEM (c) is nearly equal to that of S-FEM (a) from the viewpoint of not only the distribution but the magnitude. Non-slip condition at the inner boundary is reproduced by the local enrichment for the velocity in spite of not being applied any essential boundary conditions. In contrast to the desirable result of the X-FEM, that of the V-FEM (b) shows a serrated contour near the inner hole that arises from the voxel treatment of the non-slip boundary condition. The magnitude of the velocity of the V-FEM solution is smaller than that of the S-FEM and the X-FEM solutions by about 10% all over the domain. This result indicates that permeability tensor obtained as a volume average of the characteristic velocities is underestimated by about 10%. This data is shown in the next comparison data of homogenization.

The reason why the serrated contour of the V-FEM appears is explained in Fig. 9. The chain line is the actual surface of the inner hole, and the solid line is the one that are defined by the voxel approximation using in-and-out side judgment of element gravity centers. The dash line approximates the zero-velocity surface of the voxel-type mesh where the (bi-)linear finite element interpolation is supposed to be applied to. In this case, the zero-velocity surface reproduced by the V-FEM becomes slightly bigger than the actual one depending on the size of the finite element, and

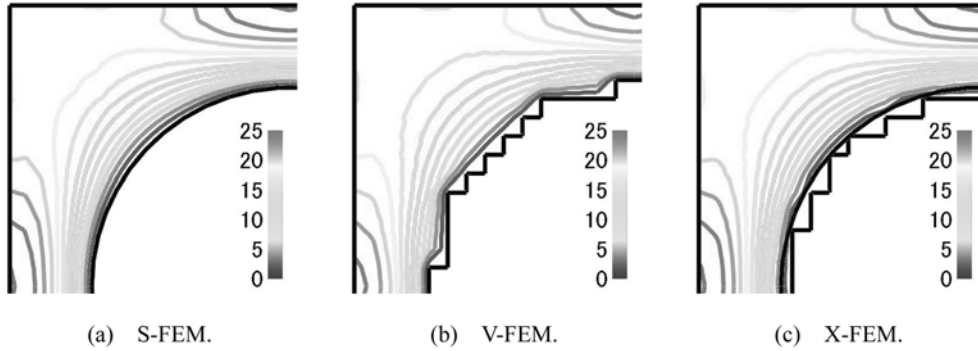


Fig. 8. Colored norm contours of localized fluid velocity (m/s)

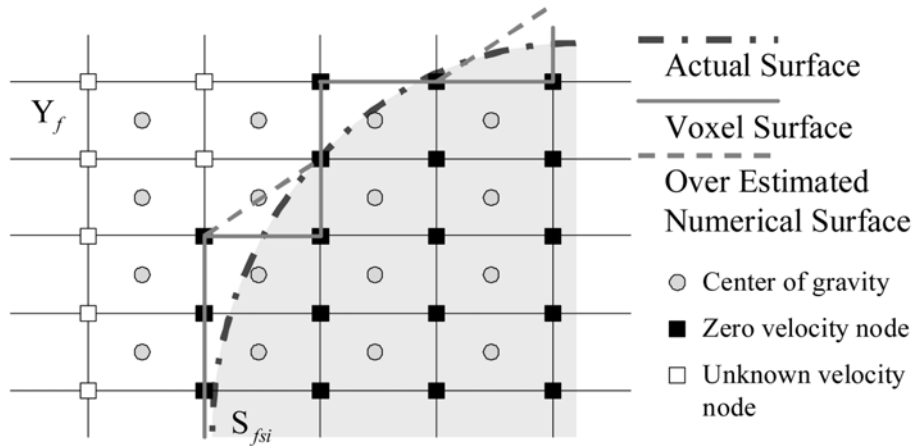


Fig. 9 Voxel approximation of the interface

of course, the converse situation is possible to take place depending on the position between the actual surface and voxel finite elements. This situation is observed in Fig. 8(b). Hence, the V-FEM has a somewhat random dependency on the size of the finite elements used in the analysis. The mesh dependency will cause the instability in the evaluation of the trade-off relation that is our target of the study. This is the reason why we introduce the X-FEM approach to the microstructure analysis rather than the V-FEM approach.

4.3 Homogenization performance

Next important factors are spatial convergence performance to the finite element mesh divisions, and its stability to the topology changes between the interface and the mesh, because we suppose to apply the method to optimal sizing and shape designs of the micro-scale structure of ceramic filters in the future stage, where the topology change between the interface and the mesh will take place with every iteration process of the optimal computations. Although the stability factor is already discussed in the localization benchmark, we show the spatial convergence performance of the three methods by changing the finite element divisions per side from 10 to 100 for all method meshes in order to check them at the same time. Fig. 6 shown above corresponds to the case of 30 divisions per side.

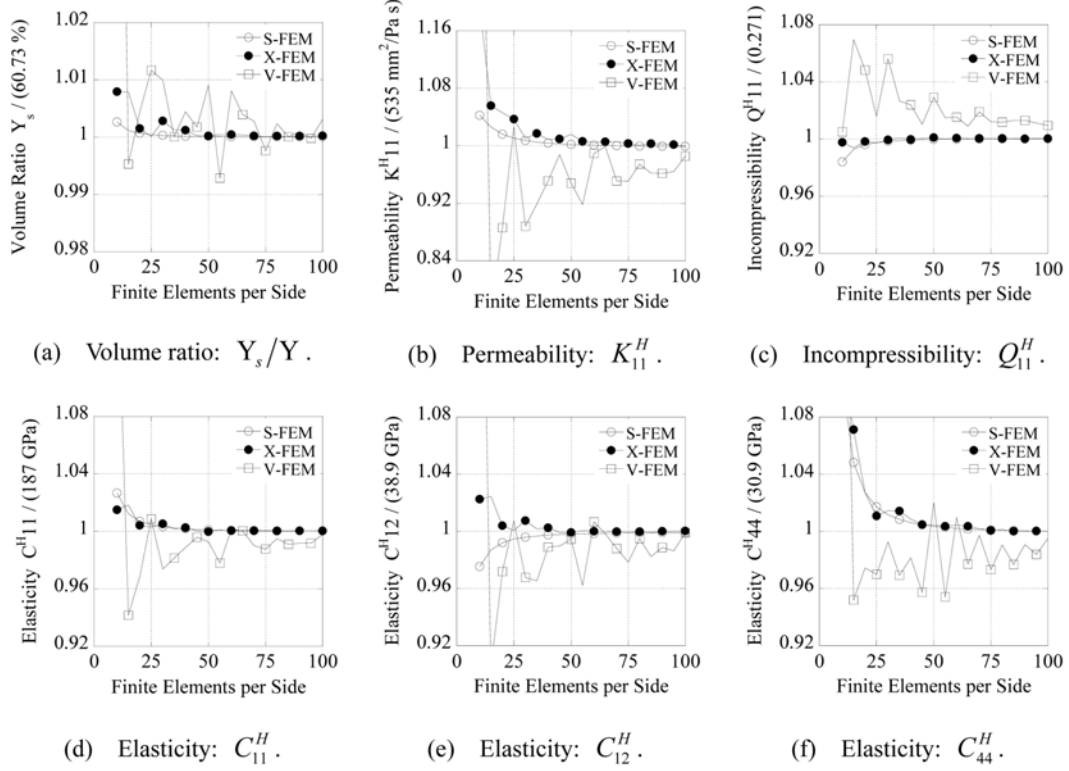


Fig. 10 Spatial convergence performances of S-FEM, V-FEM, and X-FEM

Fig. 10 shows the spatial convergence and stability of the volume ratio and the fundamental components of the homogenized permeability and elasticity tensors of the three methods. The volume ratio of Fig. 10(a) is scaled by the theoretical value of $Y_s/Y = 60.73\%$. K_{11}^H and Q_{11}^H are the first diagonal component of the permeability tensor and incompressibility compliance tensor for volume change of the solid-fluid mixtures, respectively. The others are the rigidity for the stretching C_{11}^H , coupling C_{12}^H , and shearing deformations C_{44}^H , respectively, whose indexes are written in the Voigt form for the fourth order tensor C^H . The tensor data are all normalized by the respective converged values. The converged values are as follows:

$$K_{11}^H = 535 \text{ mm}^2 / \text{Pas}, Q_{11}^H = 0.271$$

$$C_{11}^H = 187 \text{ GPa}, C_{12}^H = 38.9 \text{ GPa}, C_{44}^H = 30.9 \text{ GPa}$$

Other tensor components with non-zero values are given as follows:

$$K_{11} = K_{22}, Q_{11} = Q_{22}, C_{11} = C_{22}, C_{12} = C_{21}, C_{44} = C_{55} \quad (48a,b,c)$$

From Fig. 10, it is shown that every solution of X-FEM has a nearly comparable performance to the S-FEM not only in the spatial convergence but also in the stability. In contrast to the stable response of the X-FEM to the change of divisions, that of the V-FEM shows oscillation tendencies in all cases, and the convergence performance is not good particularly in the case of the permeability matrix (b) as already discussed in the localization benchmark. This instability results

from the voxel-type treatment of the non-slip velocity condition at the interface as explained in Fig. 9. The instability is the most one that we want to avoid. However, the results of the V-FEM are allowable in the sense of their magnitude.

From these results, we have reached the conclusion that the proposed X-FE approach has the computational advantages to the S-FEM and V-FEM in evaluation of the rigidity and permeability of the BCC- and FCC-like microstructures that are introduced to extract the effects of the depth of the neck part of the sintered particles as shown in Fig. 1(a) as the idealized model of the actual microstructure of Fig. 1(b). The X-FEM does not need to construct the interface-fitted meshes, and it has an allowable accuracy and stability in the evaluation.

5. Three-dimensional extraction analysis using BCC and FCC microstructures

In this section, we show the three-dimensional analysis of the body-centered cubic (BCC) and face-centered cubic (FCC) models of the microstructure of the partially sintered ceramic filter in order to extract the effects of the neck depth of the sintered ceramic particles of Fig. 1(a) without random and uncontrollable factors of the actual microstructure as shown in Fig. 1(b). We have large interests on how the sintered part of the small ceramic particles exerts on the macroscopic rigidity and permeability of the ceramics filters so that we can reflect the computational results in developing the fabrication technique of the particle type ceramics filters.

5.1 Problem set-up

A two-dimensional-like illustration of the BCC model is shown in Fig. 11, and that of the FCC is omitted in this paper because of similarity between the two structures. Responses of the macroscopic rigidity and permeability evaluated from the two models are examined as functions of the distance between the two ceramic particles d . The distance is defined as that from the corner to body-center particles for the BCC model as shown in Fig. 11, while it is defined by the corner to face-center particles in the FCC model.

To extract the responses of the macroscopic rigidity and permeability to the distance, we change it from $0.87D$ to $0.05D$ with the diameter of the ceramic particle fixed as $D = 1.0$ mm. Four representative configurations of the BCC and FCC models are displayed in Figs. 12 and 13, respectively. The sintered parts become bigger as the scaled distance decreases. The situation when the scaled distance d/D introduced here becomes 1.0 corresponds to the standard BCC and FCC structures where the corner and body/face-center particles contacts at the point theoretically, while the corner particles collide with each other when $d/D = \sqrt{3}/2 \approx 0.87$ in the BCC model theoretically. However, these situations take place at a little longer scaled length in the numerical analysis due to the level set representation of the critical contacting point as shown in Figs.12 and 13. We consider that the gap between the theoretical and numerical values does not present critical problems for the extraction analysis, because we need the tendency but the point-wise accuracy. This will become a future theme of the proposed method. This point is discussed in Wagner *et al.* 2003. As a remark to the homogenization analysis, fluid and solid phases are distinguished distinctly in the three-dimensional applications. This treatment differs from the previous two-dimensional benchmark analysis. The solid phase corresponds to the particle domains of the unit cells, and the fluid phases to their gap domains.

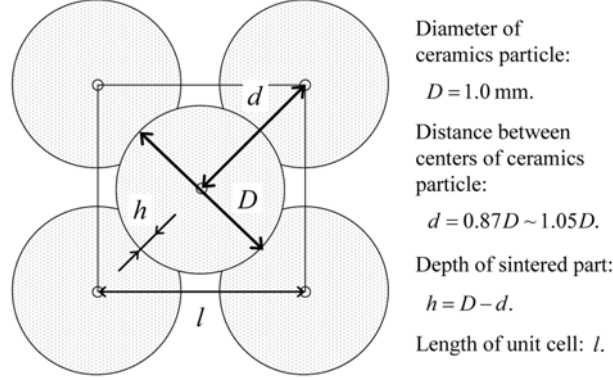


Fig. 11 Sectional illustration of body-centered cubic (BCC) model for partially-sintered ceramic particles

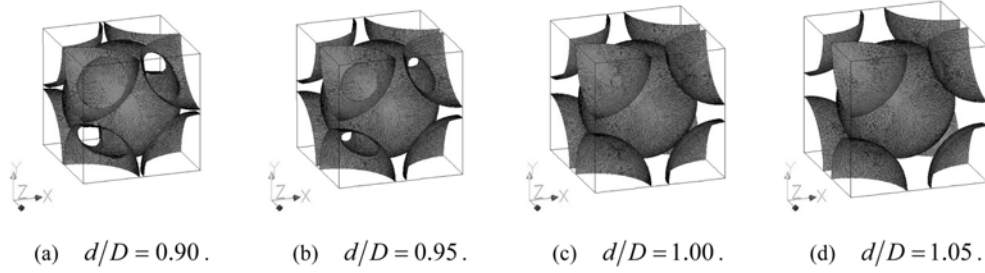


Fig. 12 BCC unit cells of the four representative value of d/D s

5.2 Trade-off relationship between permeability and rigidity

Fig. 14 shows the response curves obtained by the homogenization analysis with the proposed method. The finite element mesh used in the analysis is shown in Fig.15(a). The finite elements per each direction are 34. Material parameters are $E_s = 420$ GB, $\nu_s = 0.25$, and $\mu_f = 18.22$ mPa s. The homogenization tensors Q_{11}^H , K_{11}^H , C_{11}^H , C_{12}^H , and C_{44}^H are the same components as the previous two-dimensional benchmark. Original values of the three rigidity components are respectively defined as:

$$C_{11} = \frac{E(1-\nu)}{(1+\nu)(1-2\nu)}, \quad C_{12} = \frac{E\nu}{(1+\nu)(1-2\nu)}, \quad C_{44} = \frac{E}{2(1+\nu)} \quad (49a,b,c)$$

Other components with non-zero values are given as follows considering the asymmetric geometry:

$$K_{11} = K_{22} = K_{33}, \quad Q_{11} = Q_{22} = Q_{33} \quad (50a,b)$$

$$C_{11} = C_{22} = C_{33}, \quad C_{12} = C_{21} = C_{23} = C_{32} = C_{31} = C_{13}, \quad C_{44} = C_{55} = C_{66} \quad (50c,d,e)$$

With respect to the three homogenized elasticities of Fig. 14, they decrease as nearly proportional but nonlinear functions of the ceramic particles distance, while the permeability increases with a nearly squared curve. It has become clear that the nonlinearity of the BCC results comes from the topology changes as shown in Fig. 12. With the increase of the scaled distance, eight corner

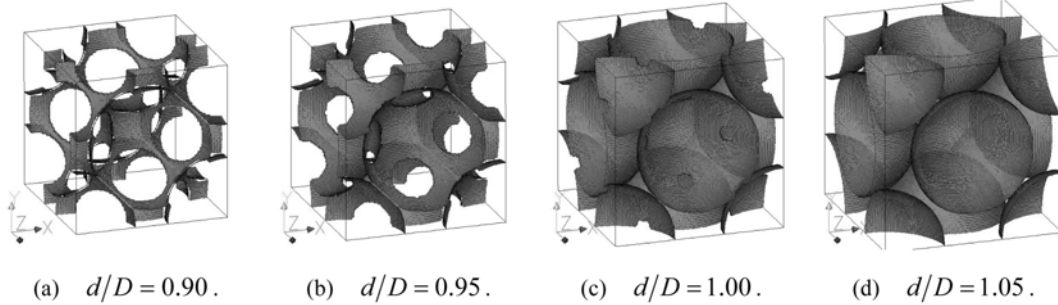


Fig. 13 FCC unit cells of the four representative value of d/D s

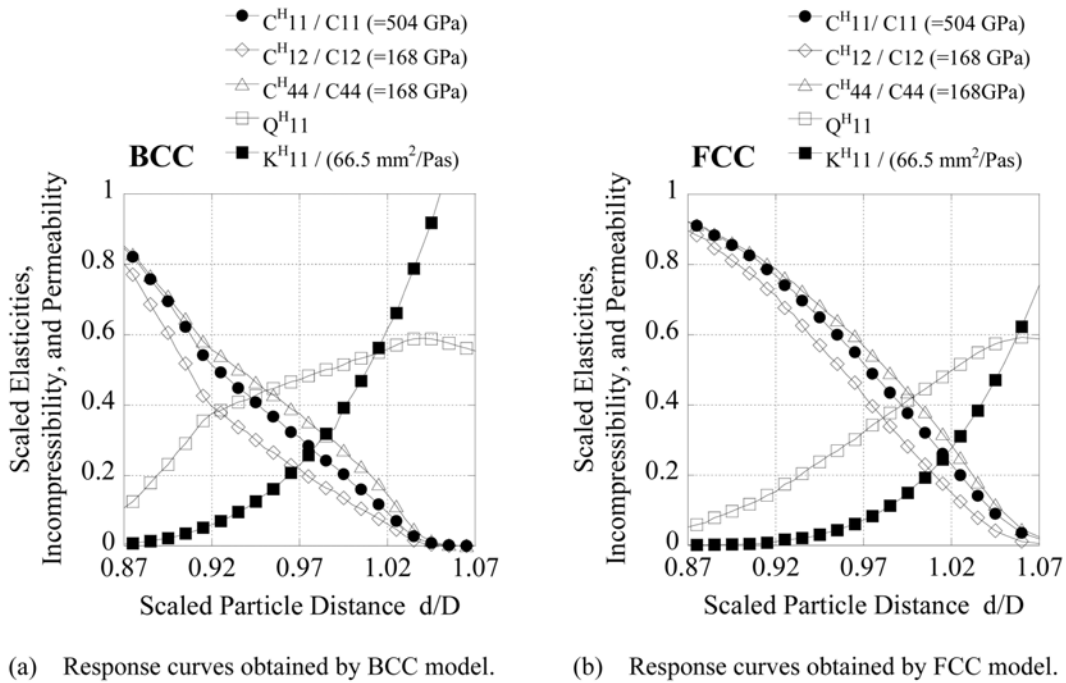


Fig. 14 Homogenized elasticity, incompressibility, and permeability matrix components as functions of distance between center and body/face-centered particles

particles of the BCC unit cell gradually separate with each other. The separating point is observed as the C1 discontinuity of the response curve of Fig. 12 around the 0.92 scaled distance. When the scaled distance becomes nearly large than 1.05 as shown in the respective sub-figures (c) and (d) of Figs. 12 and 13, the homogenized elasticities become zero due to the no existence of the sintered parts of the particles. By contrast, response curves of the FCC model are comparatively smooth, because the topology changes do not take place within the present ledge of the scaled distance except for over 1.05 area. This tendency also applies to the compliance for the volume change Q_{11}^H . And then, we can obtain from the response curves that the rigidity of the FCC microstructure is larger than that of the BCC microstructure, and the permeability is smaller. These response curves

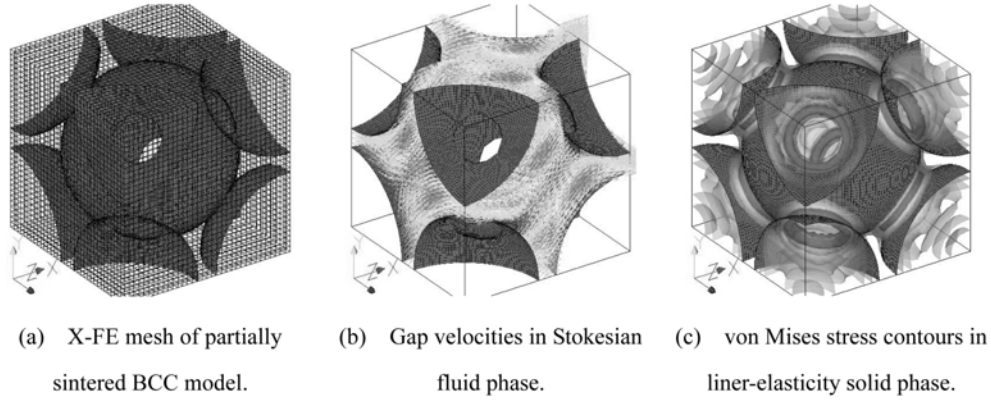


Fig. 15 Three-dimensional application to BCC unit cell model of partially-sintered ceramic particles

become a useful guideline on fabricating the particle-type ceramic filter of Fig. 1(b). For instance, the permeability efficient of the BCC model becomes a quarter of some reference value if we want to obtain twice-large magnitude of the rigidity.

In the computational aspect, if we try to obtain the response curves with the S-FEM, we are required to generate interface-fitted meshes at every plotting point. In the X-FEM, we have only to update nodal level set values using a common voxel-type mesh. This is an essential merit of introducing local enrichments for primitive variables.

5.3 Temporal localization example

The temporal localization results that are carried out for the BCC microstructure with the same values of the previous two-dimensional application are shown in Fig. 15. This is the case of $d/D = 0.97$. Fig. 15(b) shows velocity vectors in the fluid phase, and (c) the von Mises stress contours of the ceramics phases. These localization results show good behaviors as well as the pervious two-dimensional benchmark simulation. The gap velocities satisfy non-slip conditions at the complex interface between the two-phases. We can observe that the von Mises stress, which will become an indicator of plasticity failures and fatigues, concentrates near the sintered parts. From these three-dimensional applications, it is shown that the enrichment function introduced to meet the interface conditions is applicable to such three-dimensional cases without other additional numerical techniques.

6. Summary and concluding remarks

In this paper, we have proposed the way of handling the complex microstructures with solid and fluid phases without the usage of interface-fitted meshes. This method is a combined approach of the homogenization method for solid-fluid mixtures and the eXtended finite element method (X-FEM). The method introduces local enrichment functions that automatically meet interface conditions between the solid and fluid phases without additional constraint equations. A two-dimensional simple benchmark simulation shown in the paper demonstrated that the proposed

method has a comparable performance to the standard interface-fitted mesh approach (S-FEM) not only in the homogenization aspect but also in the localization, and surpasses the voxel-type mesh approach (V-FEM) in the simple two-dimensional benchmark.

The developed method is supposed to be used for the computer-aided optimal design of ceramic filters fabricated with partial sintering technique of spherical particles or powders in a future stage. We have shown that the method is applicable to the body-centered cubic (BCC) and face-centered cubic (FCC) models of the microstructure of the ceramic filter without other additional techniques. Using this method, we have revealed that, for instance, the rigidity of the BCC microstructures decrease nearly proportional to the ceramic particles distance that reflects the level of the partial sintering, while the permeability increases with a squared curve. This means that the permeability efficient of the BCC model becomes a quarter of some reference value if we want to obtain twice-large magnitude of the rigidity. These response curves obtained in this study will become a useful data in fabricating the actual particle-type ceramic filters.

As a concluding remark from another viewpoint of the study, this paper provided not only the X-FEM approach to the evaluation of the trade-off relationship but also the numerical accuracy and stability of the usual S-FEM and V-FEM approaches. After reading this paper, if the readers judge the X-FEM is too much for the homogenization method, and the accuracy and stability of the V-FEM are insufficient or allowable, we recommend using the V-FEM because of the low cost of the implementation. This paper gives a criterion for judging it.

Acknowledgements

We would like to thank Prof. Kenjiro Terada at Tohoku University, Japan, for helpful discussions about the homogenization method for solid-fluid mixtures.

References

- Belytschko, T., Moës, N., Usui, S. and Parimi, C. (2001), "Arbitrary discontinuities in finite elements", *Int. J. Numer. Meth. Eng.*, **50**, 993-1013.
- Biot, M.A. (1956), "Theory of deformation of a porous viscoelastic anisotropic solid", *J. Appl. Phys.*, **27**, 59-467.
- Fukushima, M., Zhou, Y., Nakata, M. and Yoshizawa, Y. (2008), "Fabrication of porous silicon carbide with controlled submicrometer pore", *Mat. Sci. Eng., B*, **143**, 211-214.
- Greskovich, C. and Lay, K.W. (1972), "Grain growth in very porous Al₂O₃ compacts", *J. Am. Ceram. Soc.*, **55**, 142-146.
- Guest, J.K. and Prévost, J.H. (2006), "Optimizing multifunctional materials: Design of microstructures for maximized stiffness and fluid permeability", *Int. J. Solids Struct.*, **43**, 7028-7047.
- Hardy, D. and Green, D.J. (1995), "Mechanical properties of a partially sintered alumina", *J. Euro. Ceram. Soc.*, **15**, 769-775.
- Hornung, U. (1997), "Homogenization and porous media", *Interdisciplinary Applied Mathematics*, **6**, Springer.
- Ikeda, Y., Nagano, Y., Kawamoto, H., and Takano, N. (2004), "Image-based modeling and stress analysis by homogenization method for porous aluminacermics", *J. Ceram. Soc. Japan*, **112**(5), 1052-1058.
- Isobe, T., Kameshima, Y., Nakajima, A., Okada, K. and Hotta, Y. (2007), "Gas permeability and mechanical properties of porous alumina ceramics with unidirectionally aligned pores", *J. Eur. Ceram. Soc.*, **27**, 53-59.
- Johnson, A.A., Tezduyar T.E. (1999), "Advanced mesh generation and update methods for 3D flow simulations", *Comput. Mech.*, **23**, 130-143, 1999.

- Krenar, S., Mottern, M.L., Yu, D., and Verweij, H. (2006), "Preparation and properties of porous α -Al₂O₃ membrane supports", *J. Am. Ceram. Soc.*, **89**, 1790-1794.
- Legay, A., Chessa, J. and Belytschko, T. (2006), "An Eulerian-Lagrangian method for fluid-structure interaction based on level sets", *Comput. Methods Appl. Mech. Eng.*, **195**, 2070-2087.
- Lin, Y.-S. and Burggraaf, A.J. (1991), "Preparation and characterization of high-temperature thermally stable alumina composite membrane", *J. Am. Ceram. Soc.*, **74**, 219-224.
- Lin, P.-K. and Tsai, D.-S. (1997), "Preparation and analysis of a silicon carbide composite membrane", *J. Am. Ceram. Soc.*, **80**, 365-372.
- Moës, N., Dolbow, J., and Belytschko, T. (1999), "A finite element method for crack growth without remeshing", *Int. J. Numer. Meth. Eng.*, **46**, 131-150.
- Moës, N., Cloirec, M., Cartraud, P. and Remacle, J.-F. (2003), "A computational approach to handle complex microstructure geometries", *Comput. Methods Appl. Mech. Eng.*, **192**, 3163-3177.
- Murad, M.A., Guerreiro, J.N. and Loula, A.F.D. (2001), "Micromechanical computational modeling of secondary consolidation and hereditary creep in soils", *Comput. Methods Appl. Mech. Eng.*, **190**, 1985-2016.
- Nagashima, T., Omoto, Y., and Tani, S. (2003), "Stress intensity factor analysis of interface cracks using X-FEM", *Int. J. Numer. Meth. Eng.*, **56**, 1151-1173, 2003.
- Nanjangud, S.C. and Green, D.J. (1995), "Mechanical behavior of porous glasses produced by sintering of spherical particles", *J. Euro. Ceram. Soc.*, **15**, 655-660.
- Sawada, T., Nakasumi, S. and Tezuka, A. (2007a), "Optimization of micro-structure in ceramic filter with two-scale X-FEM", *Proceedings of the 21st Canadian Congress of Applied Mechanics (CANCAM 2007)*, 102-103, Toronto, Canada, June.
- Sawada, T., Yoshizawa, Y. and Tezuka, A. (2007b), "Extended finite element discretization technique of the solid-fluid mixture homogenization method forward two-scale optimal design of fluid permeation filters", *Proceedings of the 3rd Asian-Pacific Congress on Computational Mechanics (APCOM'07) in conjunction with EPMESC XI*, 1-10, Kyoto, Japan, December.
- Sawada, T. and Hisada, T. (2007c), "Fluid-structure interaction analysis of the two-dimensional flag-in-wind problem by an interface-tracking ALE finite element method", *Comput. Fluids*, **36**, 136-146.
- Sawada, T., Tezuka, A. and Hisada, T. (2007d), "Extended finite element method for the fluid-structure interaction problems based on discontinuous interpolations on level set interfaces", *Proceedings of the 3rd Asian-Pacific Congress on Computational Mechanics (APCOM'07) in conjunction with EPMESC XI*, 1-10, Kyoto, Japan, December.
- Stein K., Tezduyar T., Benney R. (2003), "Mesh moving techniques for fluid-structure interactions with large displacements", *J. Appl. Mech.*, **70**, 58-63.
- Suwanmethanond, V., Goo, E., Liu, P.K.T., Johnston G., Sahimi, M., and Tsotsis, T.T. (2000), "Porous silicon carbide sintered substrates for high-temperature membranes", *Ind. Eng. Chem. Res.*, **39**, 3264-3271.
- Takano, N., Zako, M., Okazaki, T., Terada, K., (2002), "Microstructure-based evaluation of the influence of woven architecture on permeability by asymptotic homogenization theory", *Compos. Sci. Tech.*, **62**, 1347-1356.
- Takano, N., Zako, M., Kubo, F., Kimura, N., (2003a), "Microstructure-based stress analysis and evaluation for porous ceramics by homogenization method with digital image-based modeling", *Int. J. Solids Struct.*, **40**, 1225-1242.
- Takano, N., Kimura, K., Zako, M., and Kubo, F. (2003b), "Three-dimensional microstructural modeling and homogenization of porous alumina with needle-like pores", *JSME Int. J., A*, **46**(3), 519-526.
- Terada, K., Ito, T. and Kikuchi, N. (1998), "Characterization of the mechanical behaviors of solid-fluid mixture by the homogenization method", *Comput. Methods Appl. Mech. Eng.*, **153**, 223-257.
- Terada, K., Asai, M. and Yamagishi, M. (2003), "Finite cover method for linear and non-linear analyses of heterogeneous solids", *Int. J. Numer. Meth. Eng.*, **58**, 1321-1346.
- Terada, K. and Kurumatani, M. (2004), "Performance assessment of generalized elements in the finite cover method", *Finite Elements Analysis Design*, **41**, 111-132.
- Tezduyar, T.E., Mittal, S., Ray, S.E. and Shih, R. (1992), "Incompressible flow computations with stabilized bilinear and linear equal-order-interpolation velocity-pressure elements", *Comput. Methods Appl. Mech. Eng.*, **95**, 221-242.

- Tezduyar, T.E. (2003), "Computation of moving boundaries and interfaces and stabilization parameters", *Int. J. Numer. Meth. Fluids*, **43**, 555-575.
- Wagner, G.J., Moës, N., Liu, W.K. and Belytschko, T. (2001), "The extended finite element method for rigid particles in Stokes flow", *Int. J. Numer. Meth. Eng.*, **51**, 293-313.
- Wagner, G.J., Ghosal, S. and Liu, W.K. (2003), "Particulate flow simulations using lubrication theory solution enrichment", *Int. J. Numer. Meth. Eng.*, **56**, 1261-1289.
- Wang, J.G., Leung, C.F. and Chow, Y.K. (2003), "Numerical solutions for flow in porous media", *Int. J. Numer. Anal. Meth. Geomech.*, **27**, 565-583.